

Simulation of capacitively coupled Ar/O_2 discharges based on global/equivalent circuit model and an extended reaction set

Yi Wang(王怡), Wan Dong(董婉), Yi-Fan Zhang(张逸凡), Liu-Qin Song(宋柳琴), and Yuan-Hong Song(宋远红)
Citation: Chin. Phys. B, 2025, 34 (**8**): 085201. DOI: 10.1088/1674-1056/add4e5
http://cpb.iphy.ac.cn; http://iopscience.iop.org/cpb

What follows is a list of articles you may be interested in

Discharge mode and particle transport in radio frequency capacitively coupled Ar/O_2 plasma discharges

Zhuo-Yao Gao(高卓瑶), Wan Dong(董婉), Chong-Biao Tian(田崇彪), Xing-Zhao Jiang(蒋星照), Zhong-Ling Dai(戴忠玲), and Yuan-Hong Song(宋远红)
Chin. Phys. B, 2024, 33 (**9**): 095203. DOI: 10.1088/1674-1056/ad5d65

Power transfer efficiency in an air-breathing radio frequency ion thruster

Gao-Huang Huang(黄高煌), Hong Li(李宏), Fei Gao(高飞), and You-Nian Wang(王友年)
Chin. Phys. B, 2024, 33 (**7**): 075201. DOI: 10.1088/1674-1056/ad426c

Diagnosing ratio of electron density to collision frequency of plasma surrounding scaled model in a shock tube using low-frequency alternating magnetic field phase shift

Ming-Xing Wu(吴明兴), Kai Xie(谢楷), Yan Liu(刘艳), Han Xu(徐晗), Bao Zhang(张宝), and De-Yang Tian(田得阳)
Chin. Phys. B, 2024, 33 (**5**): 055204. DOI: 10.1088/1674-1056/ad2d56

Global simulation of plasma series resonance effect in radio frequency capacitively coupled Ar/O_2 plasma

Xue Bai(白雪), Hai-Wen Xu(徐海文), Chong-Biao Tian(田崇彪), Wan Dong(董婉), Yuan-Hong Song(宋远红), and You-Nian Wang(王友年)
Chin. Phys. B, 2023, 32 (**12**): 125203. DOI: 10.1088/1674-1056/ace427

Measurement of electronegativity during the E to H mode transition in a radio frequency inductively coupled Ar/O_2 plasma

Peng-Cheng Du(杜鹏程), Fei Gao(高飞, Xiao-Kun Wang(王晓坤), Yong-Xin Liu(刘永新), and You-Nian Wang(王友年)
Chin. Phys. B, 2021, 30 (**3**): 035202. DOI: 10.1088/1674-1056/abccb0

Simulation of capacitively coupled Ar/O_2 discharges based on global/equivalent circuit model and an extended reaction set

Yi Wang(王怡), Wan Dong(董婉), Yi-Fan Zhang(张逸凡),
Liu-Qin Song(宋柳琴), and Yuan-Hong Song(宋远红)†

Key Laboratory of Materials Modification by Laser, Ion and Electron Beams (Ministry of Education), School of Physics, Dalian University of Technology, Dalian 116024, *China*

(Received 12 March 2025; revised manuscript received 16 April 2025; accepted manuscript online 7 May 2025)

Radio frequency capacitively coupled plasmas (RF CCPs) operated in Ar/O_2 gas mixtures which are widely adopted in microelectronics, display, and photovoltaic industry, are investigated based on an equivalent circuit model coupled with a global model. This study focuses on the effects of singlet metastable molecule $O_2\left(b^1\Sigma_g^+\right)$, highly excited Herzberg states $O_2\left(A^3\Sigma_u^+, A^3\Delta_u, c^1\Sigma_u^-\right)$, and the negative ion O_2^-, which are usually neglected in simulation studies. Specifically, their impact on particle densities, electronegativity, electron temperature, voltage drop across the sheath, and absorbed power in the discharge is analyzed. The results indicate that $O_2\left(b^1\Sigma_g^+\right)$ and O_2^- exhibit relatively high densities in argon–oxygen discharges. While $O_2\left(A^3\Sigma_u^+, A^3\Delta_u, c^1\Sigma_u^-\right)$ play a critical role in $O_2\left(b^1\Sigma_g^+\right)$ production, especially at higher pressure. The inclusion of these particles reduces the electronegativity, electron temperature, and key species densities, especially the O^- and O^* densities. Moreover, the sheath voltage drop, as well as the inductance and resistance of the plasma bulk are enhanced, while the sheath dissipation power and total absorbed power decrease slightly. With the increasing pressure, the influence of these particles on the discharge properties becomes more significant. The study also explores the generation and loss of main neutral species and charged particles within the pressure range of 20 mTorr–100 mTorr (1 Torr = 1.33322×10^2 Pa), offering insights into essential and non-essential reactions for future low-pressure O_2 and Ar/O_2 CCP discharge modeling.

Keywords: Ar/O_2 CCP discharges, reaction set, equivalent circuit model, global model

PACS: 52.27.Cm, 52.65.–y, 52.80.Pi, 82.33.Xj

DOI: 10.1088/1674-1056/add4e5 **CSTR:** 32038.14.CPB.add4e5

1. Introduction

Capacitively or inductively coupled Ar/O_2 gas mixture discharges have broad application prospects in ashing of photoresist, etching of metals, and polycrystalline silicon, plasma-enhanced deposition of silicon dioxide processes.[1–4] It is well known that abundant active particles, including electrons, various ions, and neutral species, which play different roles in plasma treatment processes, can be generated in Ar/O_2 plasmas via complicated chemical channels. For example, neutral particles in plasmas have garnered significant attention due to their critical role in plasma chemical reactions and surface material processes.[5–9] In Qu *et al.*'s study,[1] it is demonstrated that the primary neutral radicals related to oxygen discharges are atomic oxygen in ground state O, metastable atomic oxygen O^*, singlet delta metastable $O_2\left(a^1\Delta_g\right)$ and $O_2\left(b^1\Sigma_g^+\right)$, in plasma-enhanced atomic layer deposition of SiO_2 film. Besides, it should be noticed that collisions with singlet delta metastable states in many cases have larger cross sections and thus higher reaction rates than corresponding collisions with the ground state molecule. Therefore, $O_2\left(a^1\Delta_g\right)$ and $O_2\left(b^1\Sigma_g^+\right)$ are expected to play significant roles in oxygen discharges. Additionally, the presence of negative ions would alter the overall discharge mechanism with additional volume recombination loss, and particular spatial distribution of negative ions may affect the ion flux loss to the wall.[10,11]

However, some neutral particles are usually neglected in previous simulation studies. For example, $O_2\left(b^1\Sigma_g^+\right)$ was often reported in small concentrations[9,12] in oxygen discharges. One reason would be the wall quenching which was regarded as the major loss channel for $O_2\left(b^1\Sigma_g^+\right)$ and $O_2\left(a^1\Delta_g\right)$ metastable species. Meanwhile, the wall quenching of $O_2\left(b^1\Sigma_g^+\right)$ was reported as being much higher than the $O_2\left(a^1\Delta_g\right)$.[13,14] Therefore, $O_2\left(b^1\Sigma_g^+\right)$ density was considered to be much lower than $O_2\left(a^1\Delta_g\right)$ in previous simulation studies. Nevertheless, the wall quenching of $O_2\left(b^1\Sigma_g^+\right)$ might be overestimated based on studies by Andrea.[15] Also, more importantly, some $O_2\left(b^1\Sigma_g^+\right)$ related reactions, such as $O^* + O_2 \rightarrow O + O_2\left(b^1\Sigma_g^+\right)$, were usually neglected previously.[9,12,16] Thus, the $O_2\left(b^1\Sigma_g^+\right)$ density and related reaction rates involving $O_2\left(b^1\Sigma_g^+\right)$ are tended to be underestimated. Recent investigation based on global model has demonstrated the substantial presence of $O_2\left(b^1\Sigma_g^+\right)$ in O_2 ICP discharges,[17] in which $O_2\left(A^3\Sigma_u^+, A^3\Delta_u, c^1\Sigma_u^-\right)$ is also shown to contribute to $O_2\left(b^1\Sigma_g^+\right)$ generation. Recent experimental and simulation efforts also underscored the signifi-

†Corresponding author. E-mail: songyh@dlut.edu.cn

© 2025 Chinese Physical Society and IOP Publishing Ltd. All rights, including for text and data mining, AI training, and similar technologies, are reserved.

cance of metastable oxygen molecule $O_2\left(b^1\Sigma_g^+\right)$ in O_2 CCP discharges.[7,8] It was found that $O_2\left(b^1\Sigma_g^+\right)$ exerts a notable influence on O^- density, electronegativity, electron temperature, and discharge modes. This is primarily attributed to the electron detachment from negative ion O^- by the singlet molecular metastable $O_2\left(b^1\Sigma_g^+\right)$, which is considered as a crucial loss process for negative oxygen ions. Hence, incorporating $O_2\left(b^1\Sigma_g^+\right)$ into the updated Ar/O_2 reaction set becomes essential. In addition, oxygen discharges are usually weakly electronegative, and O_2^+, e, and negative ions are expected to contribute significantly to the overall charge balance in oxygen plasma. As the reaction set of oxygen discharges keeps supplementing, O_2^- has been paid more and more attention. Toneli[17] revised the O_2^--related reactions, rate coefficients for the oxygen ICP discharge, indicating that as the pressure increases, densities of O^- and O_2^- become much closer, and are nearly equal at 100 mTorr. Therefore, it is necessary to include O_2^- in the new Ar/O_2 reaction set.

The operation conditions have a significant influence on generation and loss of active species in capacitively coupled O_2 and Ar/O_2 plasmas,[18–28] essentially the reaction mechanisms. However, due to the complexity of reactions and the continual revision and update of relevant particle reaction rates,[9,17] there is presently a lack of systematic studies on how to distinguish and summarize the main reactions in O_2 and Ar/O_2 plasmas. Obviously, there is limited studies on how the existence of $O_2\left(b^1\Sigma_g^+\right)$ and O_2^- may affect the discharge characteristics. Therefore, our study in this work tries to explore the formation and annihilation of $O_2\left(b^1\Sigma_g^+\right)$, O_2^- and emphasize the impact of the new reaction set on capacitively coupled argon–oxygen mixed gas discharges. Additionally, in this study, $O_2\left(A^3\Sigma_u^+, A^3\Delta_u, c^1\Sigma_u^-\right)$ is also considered.

In this work, we study the roles of particles as well as their generation and loss mechanisms in capacitively coupled Ar/O_2 discharges using a nonlinear equivalent circuit coupled with a global model. The article structure is as follows: Section 2 provides a concise overview of the simulation model. Section 3 delves into the results analysis, and concluding remarks are presented in the final section.

2. Model description

Typical CCPs, with RF voltage applied to one of the two parallel electrodes, consist of two sheaths with bulk plasma between them. The plasma can be equivalently regarded as a series of LCR elements by using the equivalent circuit model.[29–34] With the consideration of both ohmic and stochastic heating, the effective collision rate[29,30] is given as

$$\nu_{\mathrm{eff}} = \nu_{\mathrm{m}} + \frac{\bar{v}_{\mathrm{e}}}{l_{\mathrm{p}}}, \tag{1}$$

where $\bar{v}_{\mathrm{e}}$ is the mean thermal velocity, ν_{m} indicates the momentum transfer collision frequency, l_{p} is the length of the plasma bulk. The RF sheath is modeled as a parallel connection of a constant current source, a diode, and a nonlinear capacitor.[31,32] Since we assume the ion density in the sheath is homogeneous, the sheath voltage drop for the grounded electrode and the driving electrode $V_{\mathrm{s,g}}$, $V_{\mathrm{s,p}}$ in Eq. (2) is related to the sheath charge Q_{s},[29,30,35] as

$$V_{\mathrm{s,p}} = V_{\mathrm{s,g}} = Q_{\mathrm{s}}^2/2e\varepsilon_0 n_{\mathrm{i}}^+ A^2, \tag{2}$$

where ε_0 is the vacuum permittivity, n_{i}^+ is the positive ion density, A is the electrode area. According to Kirchoff's law, the model consists of a system of the first-order nonlinear differential equations for the voltage drop across the sheath and the radio frequency current I_{rf}, the bias sheath capacitor voltage $V_{C_{\mathrm{B}}}$, with the inductance of the plasma bulk L_{p}, the ion current flowing onto the surface $I_{\mathrm{i,g}}$, $I_{\mathrm{i,p}}$, the electron current $I_{\mathrm{e,g}}$, $I_{\mathrm{e,p}}$ for the grounded electrode and the driving electrode, as

$$\frac{\mathrm{d}V_{\mathrm{s,p}}}{\mathrm{d}t} = -(I_{\mathrm{rf}} + I_{\mathrm{i,p}} - I_{\mathrm{e,p}})C_{\mathrm{s,p}}^{-1}, \tag{3}$$

$$\frac{\mathrm{d}V_{\mathrm{s,g}}}{\mathrm{d}t} = -\left(-I_{\mathrm{rf}} + I_{\mathrm{i,g}} - I_{\mathrm{e,g}}\right)C_{\mathrm{s,g}}^{-1}, \tag{4}$$

$$\frac{\mathrm{d}I_{\mathrm{rf}}}{\mathrm{d}t} = \left(V_{\mathrm{rf}} + V_{C_{\mathrm{B}}} + V_{\mathrm{s,p}} - V_{\mathrm{s,g}}\right)L_{\mathrm{p}}^{-1} - \nu_{\mathrm{eff}} I_{\mathrm{rf}}, \tag{5}$$

$$\frac{\mathrm{d}V_{C_{\mathrm{B}}}}{\mathrm{d}t} = -I_{\mathrm{rf}} C_{\mathrm{B}}^{-1}. \tag{6}$$

The sheath dissipation and absorbed power are calculated from I_{rf}, $V_{\mathrm{s,g}}$, $V_{\mathrm{s,p}}$, and the plasma potential V_{rf}, as

$$P_{\mathrm{sheath}} = \frac{1}{T}\int \left(V_{\mathrm{s,g}}(t) - V_{\mathrm{s,p}}(t)\right) I_{\mathrm{rf}}(t)\,\mathrm{d}t, \tag{7}$$

$$P_{\mathrm{abs}} = \frac{1}{T}\int V_{\mathrm{rf}}(t) I_{\mathrm{rf}}(t)\,\mathrm{d}t. \tag{8}$$

The equivalent circuit of the plasma region is simplified to a series connection of an inductance L_{p} and a resistance R_{p}. Based on this model, the absorbed power related to Ohmic heating P_{ohm} and stochastic heating P_{stoc} can be calculated from the RF plasma currents[35–38] as

$$P_{\mathrm{ohm}} = \langle \nu_{\mathrm{m}} L_{\mathrm{p}} I_{\mathrm{rf}}^2 \rangle, \tag{9}$$

$$P_{\mathrm{stoc}} = \langle \nu_{\mathrm{e}} L_{\mathrm{p}} I_{\mathrm{rf}}^2 / l_{\mathrm{p}} \rangle. \tag{10}$$

The determination of the electron density, electron temperature, and ion density in CCP global model is mainly achieved by means of the energy balance equation, the particle number balance equation, and the quasi-neutrality condition.[39–41] The diffusional losses of neutral particles to the reactor walls are estimated by an effective loss-rate coefficient, which are given as

$$K_{\mathrm{loss}} = \left[\frac{\Lambda^2}{D} + \frac{2V_{\mathrm{bulk}}(2-\gamma)}{A v_{\mathrm{e}} \gamma}\right]^{-1}, \tag{11}$$

where D is the neutral diffusion coefficient, γ is the sticking coefficient on the wall surface, V_{bulk} is the volume of the reactor chamber, respectively, and Λ is effective diffusion length

of each of the neutral species.[9] Besides, the loss rate due to the ion flux to the walls is given by

$$K_{+,\mathrm{loss}} = u_{\mathrm{B}} \frac{A_{\mathrm{eff}}}{V}, \tag{12}$$

where u_{B} is the Bohm velocity, $A_{\mathrm{eff}} = 2\pi(R^2 h_{\mathrm{L}} + RLh_{\mathrm{R}})$ is the effective surface area for ion loss, h_{L} and h_{R} are the axial and radial edge to center positive ion density ratios, R is the chamber radius.[9]

This section outlines the simulation procedure for CCP Ar/O_2 plasma discharge, based on a nonlinear equivalent circuit model coupled with a global model, as shown in Fig. 1. The initial plasma parameters, including estimated circuit element values, are provided for transient simulation. And the currents and voltages at each branch and node are then obtained by the transient circuit calculation, allowing the absorbed power of the plasma and the averaged sheath voltage to be determined. These calculated results are then fed back into the global model to update key plasma parameters. This iterative process continues until a steady state is achieved, in which the plasma absorbed power P_{abs} reach consistent values $\left(\frac{P_{\mathrm{abs}(t)} - P_{\mathrm{abs}(t-1)}}{P_{\mathrm{abs}(t)}} \leq 10^{-3}\right)$.

In the collision reaction set, fifteen species are considered. In addition to electron, molecular oxygen in ground state O_2, metastable molecular oxygen $O_2\left(a^1\Delta_g\right)$, $O_2\left(b^1\Sigma_g^+\right)$, and the highly excited Herzberg states $O_2\left(A^3\Sigma_u^+, A^3\Delta_u, c^1\Sigma_u^-\right)$, atomic oxygen in ground state O, metastable atomic oxygen O^*, ozone O_3, positive ions O^+ and O_2^+, and negative ions O^-, O_2^- are included. Moreover, some particles related to argon are also included, such as argon atom in the ground state Ar, metastable argon Ar^* (the metastable levels $1s_5$ and $1s_3$) and positive argon ion Ar^+.

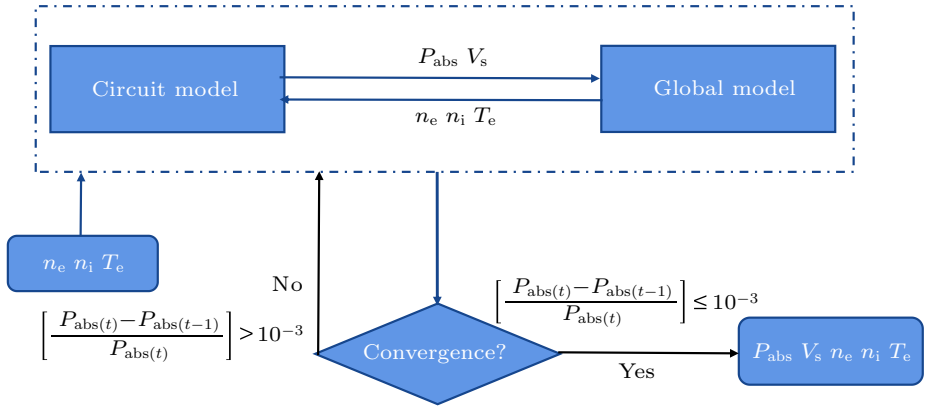


Fig. 1. Flowchart of the algorithm of the simulation.

Specific reaction sets are shown in Tables 1–3. Moreover, compared to the original reaction set for Ar/O_2 ICP, reactions R_{53} and R_{54} have been added to the set based on Gudmundsson's updated reaction set.[7,8,17] Recent investigations have demonstrated the importance of $O_2\left(b^1\Sigma_g^+\right)$, $O_2\left(A^3\Sigma_u^+, A^3\Delta_u, c^1\Sigma_u^-\right)$, and O_2^-, as mentioned before.[7,8,17] Therefore, the relevant reactions of three particles are included in Tables 2 and 3, based on the newly developed reaction set constructed by Toneli.[17] The metastable molecular oxygen $O_2\left(a^1\Delta_g\right)$, $O_2\left(b^1\Sigma_g^+\right)$, and the highly excited Herzberg states $O_2\left(A^3\Sigma_u^+, A^3\Delta_u, c^1\Sigma_u^-\right)$ are respectively represented as $O_2^*(a)$, $O_2^*(b)$, O_2^H. The wall surface reactions as well as the wall recombination and quenching coefficients are shown in Table 4. Based on the model and reaction set presented in this work, the calculated results are compared with those in Ref. [9] under the same discharge parameters, and the trends of particle densities as well as the magnitudes of individual particles densities are basically the same. This demonstrates the reliability of both the model and the reaction set employed in this study.

Table 1. Chemical reactions considered in the global model (exclude: $O_2\left(b^1\Sigma_g^+\right)$, $O_2\left(A^3\Sigma_u^+, A^3\Delta_u, c^1\Sigma_u^-\right)$, and O_2^-).

	Reactions	Rate coefficients ($m^3 \cdot s^{-1}$)	References
1	$e + Ar \rightarrow Ar + e$	a	[39]
2	$e + Ar \rightarrow Ar^* + e$	$9.73 \times 10^{-16} \times T_e^{-0.07} \times \exp(-11.69/T_e)$	[39]
3	$e + Ar \rightarrow Ar^+ + 2e$	$2.39 \times 10^{-14} \times T_e^{-0.57} \times \exp(-17.43/T_e)$	[39]
4	$e + Ar^* \rightarrow Ar^+ + 2e$	$2.05 \times 10^{-13} \times \exp(-4.95/T_e)$	[39]
5	$e + Ar^* \rightarrow Ar + e$	2.0×10^{-13}	[39]
6	$Ar^* + Ar^* \rightarrow Ar + Ar^+ + e$	6.2×10^{-16}	[39]
7	$e + O_2 \rightarrow O_2 + e$	$\exp(-30.7683 + 0.3531 \times \ln(T_e) + 0.2068 \times (\ln(T_e))^2 - 0.0406 \times (\ln(T_e))^3$	[39]
8	$e + O_2 \rightarrow O + O + e$	$4.23 \times 10^{-15} \times \exp(-5.56/T_e)$	[39]
9	$e + O_2 \rightarrow +O^* + e$	$5.0 \times 10^{-14} \times \exp(-8.4/T_e)$	[39]
10	$e + O_2 \rightarrow +O^-$	$1.07 \times 10^{-15} \times T_e^{-1.39} \times \exp(-6.26/T_e)$	[39]

Table 1. (*Continued*).

	Reactions	Rate coefficients ($m^3 \cdot s^{-1}$)	References
11	$e + O_2 \rightarrow O_2^+ + 2e$	$2.34 \times 10^{-15} \times T_e^{-1.03} \times \exp(-12.9/T_e)$	[39]
12	$e + O \rightarrow O + e$	$\exp(-30.9463 + 0.9484 \times \ln(T_e)) - 0.14158 \times (\ln(T_e))^2 - 0.0154 \times (\ln(T_e))^3$	[39]
13	$e + O \rightarrow O^* + e$	$4.47 \times 10^{-15} \times \exp(-2.286/T_e)$	[39]
14	$e + O \rightarrow O^+ + 2e$	$9.0 \times 10^{-15} \times T_e^{0.7} \times \exp(-13.6/T_e)$	[39]
15	$e + O^* \rightarrow O^+ + 2e$	$9.0 \times 10^{-15} \times T_e^{0.7} \times \exp(-11.6/T_e)$	[39]
16	$e + O^- \rightarrow O + 2e$	$1.73 \times 10^{-13} \times \exp(-5.76/T_e + 7.3/T_e^2 3.48/T_e^3)$	[39]
17	$O_2 + O^* \rightarrow O_2 + O$	4.1×10^{-17}	[39]
18	$O^* + O \rightarrow O + O$	8.1×10^{-18}	[39]
19	$O_2^+ + O^- \rightarrow O_2 + O$	$1.5 \times 10^{-13} \times (300/T_g)^{0.5}$	[39]
20	$O^+ + O^- \rightarrow O + O$	$2.7 \times 10^{-13} \times (300/T_g)^{0.5}$	[39]
21	$e + O_2^+ \rightarrow O^* + O$	$2.2 \times 10^{-14} \times (T_e)^{-0.5}$	[39]
22	$e + O_2 \rightarrow O_2^* + e$	$1.7 \times 10^{-15} \times \exp(-3.1/T_e)$	[39]
23	$e + O_2^*(a) \rightarrow +O^-$	$2.28 \times 10^{-16} \times \exp(-2.29/T_e)$	[39]
24	$e + O_2^*(a) \rightarrow O_2^+ + 2e$	$9.0 \times 10^{-16} \times \exp(-11.6/T_e)$	[39]
25	$e + O_2^*(a) \rightarrow O + e$	$4.2 \times 10^{-15} \times \exp(-4.6/T_e)$	[39]
26	$e + O_2^*(a) \rightarrow O_2 + e$	$5.6 \times 10^{-15} \times \exp(-2.2/T_e)$	[39]
27	$O^- + O \rightarrow O_2 + e$	1.4×10^{-16}	[39]
28	$O^- + O_2^*(a) \rightarrow O_3 + e$	1.0×10^{-16}	[39]
29	$e + O_3 \rightarrow O_2 + O + e$	1.4×10^{-14}	[39]
30	$e + O_3 \rightarrow O_2 + O^-$	$2.12 \times 10^{-15} \times \exp(-0.93/T_e)$	[39]
31	$O_2 + Ar^* \rightarrow O_2 + Ar$	1.12×10^{-15}	[39]
32	$O_2 + Ar^+ \rightarrow O_2^+ + Ar$	1.2×10^{-17}	[39]
33	$O_2 + Ar^* \rightarrow O + O + Ar$	5.8×10^{-17}	[39]
34	$O + Ar^* \rightarrow O + Ar$	8.1×10^{-18}	[39]
35	$O + Ar^+ \rightarrow O^+ + Ar$	1.21×10^{-17}	[39]
36	$O^- + Ar^+ \rightarrow O + Ar$	2.7×10^{-17}	[39]
37	$O_2^+ + O^- \rightarrow 3O$	$2.6 \times 10^{-14} \times (300/T_g)^{0.44}$	[9]
38	$e + O_2 \rightarrow O^+ + O^- + e$	$7.1 \times 10^{-17} \times T_e^{0.5} \times \exp(-17.0/T_e)$	[9]
39	$e + O_2 \rightarrow O^+ + O + 2e$	$1.88 \times 10^{-16} \times T_e^{1.699} \times \exp(-16.81/T_e)$	[9]
40	$O^+ + O_2 \rightarrow O_2^+ + O$	$2.1 \times 10^{-17} \times (300/T_g)^{0.5}$	[9]
41	$e + O^* \rightarrow O + e$	$8.17 \times 10^{-17} \times \exp(-0.4/T_e)$	[9]
42	$e + O_2 \rightarrow O^* + O^* + e$	$1.95 \times 10^{-16} \times T_e^{0.22} \times \exp(-12.62/T_e)$	[9]
43	$e + O_2^*(a) \rightarrow O^+ + O + 2e$	$1.88 \times 10^{-16} \times T_e^{1.699} \times \exp(-15.83/T_e)$	[9]
44	$e + O_2^*(a) \rightarrow O^* + O^-$	$9.93 \times 10^{-15} \times T_e^{1.437} \times \exp(-7.44/T_e)$	[9]
45	$O^* + O_2 \rightarrow +O_2^*(a)$	1.0×10^{-18}	[9]
46	$e + O_2^*(a) \rightarrow +O^* + e$	$1.29 \times 10^{-14} \times T_e^{0.22} \times \exp(-11.64/T_e)$	[9]
47	$O^+ + O_3 \rightarrow O_2 + O_2 + e$	1.0×10^{-16}	[9]
48	$O + O_3 \rightarrow O_2 + O_2$	$1.81 \times 10^{-17} \times \exp(2300/T_g)$	[9]
49	$O_2 + O_3 \rightarrow O_2 + O_2 + O$	$7.26 \times 10^{-16} \times \exp(11400/T_g)$	[9]
50	$O_2^*(a) + O_3 \rightarrow O_2 + O_2 + O$	$6.01 \times 10^{-17} \times \exp(-2853/T_g)$	[9]
51	$O_2^+ + O^- \rightarrow 3O$	$2.6 \times 10^{-14} \times (300/T_g)^{0.44}$	[9]
52	$e + O_2 \rightarrow O^+ + O^- + e$	$7.1 \times 10^{-17} \times T_e^{0.5} \times \exp(-17.0/T_e)$	[9]
53	$O^+ + O_2^*(a) \rightarrow O_2^+ + O$	2×10^{-17}	[17]
54	$O^- + O_2 \rightarrow O_2 + O + e$	2.4×10^{-18}	[17]
55	$O_2^*(a) + Ar^+ \rightarrow O_2^+ + Ar$	1.2×10^{-17}	[42]
56	$O^* + Ar^+ \rightarrow O^+ + Ar$	1.2×10^{-17}	[42]

Note: a refers to that the coefficient is the integral of electron impact cross sections under Maxwellian distribution.

Table 2. The reaction set involving $O_2\left(b^1\Sigma_g^+\right)$, $O_2\left(A^3\Sigma_u^+, A^3\Delta_u, c^1\Sigma_u^-\right)$.

	Reactions	Rate coefficients ($m^3 \cdot s^{-1}$)	References
57	$e + O_2^*(b) \rightarrow +O^* + e$	$3.49 \times 10^{-14} \times \exp(-4.29/T_e)$	[9]
58	$e + O_2 \rightarrow O_2^*(b) + e$	$3.24 \times 10^{-16} \times \exp(-2.218/T_e)$	[9]
59	$O^* + O_2 \rightarrow +O_2^*$	$2.56 \times 10^{-17} \times \exp(67/T_g)$	[17]
60	$e + O_2^*(b) \rightarrow O^+ + O + 2e$	$1.88 \times 10^{-16} \times T_e^{1.699} \times \exp(-15.183/T_e)$	[9]
61	$e + O_2^*(a) \rightarrow O_2^*(b) + e$	$3.24 \times 10^{-16} \times \exp(-1.57/T_e)$	[9]
62	$e + O_2^*(b) \rightarrow +O^-$	$4.19 \times 10^{-15} \times T_e^{-1.376} \times \exp(-4.54/T_e)$	[9]
63	$e + O_2^*(b) \rightarrow O_2^+ + 2e$	$2.34 \times 10^{-15} \times T_e^{1.03} \times \exp(-10.633/T_e)$	[9]
64	$e + O_2^*(b) \rightarrow 2O + e$	$6.86 \times 10^{-15} \times \exp(-4.66/T_e)$	[9]
65	$e + O_2^*(b) \rightarrow O_2 + e$	$9.72 \times 10^{-16} \times \exp(-0.591/T_e)$	[9]

Table 2. (*Continued*).

	Reactions	Rate coefficients ($m^3 \cdot s^{-1}$)	References
66	$O^- + O_2^*(b) \rightarrow O_2 + O + e$	6.9×10^{-16}	[9]
67	$O + O_2^*(b) \rightarrow + O_2^*(a)$	8.1×10^{-20}	[9]
68	$O + O_2^*(b) \rightarrow + O_2$	4×10^{-20}	[17]
69	$O_2 + O_2^*(b) \rightarrow O_2 + O_2^*(a)$	$3.79\times10^{-22}\times(300/T_g)^{-2.4}\times\exp(-281/T_g)$	[9]
70	$O_2^*(b) + Ar^+ \rightarrow O_2^+ + Ar$	1.1×10^{-16}	[42]
71	$O_2^*(b) + O_3 \rightarrow O_2 + O_2 + O$	1.5×10^{-17}	[9]
72	$e + O_2^H \rightarrow + O^* + e$	$3.49\times10^{-14}\times\exp(-1.42/T_e)$	[9]
73	$e + O_2 \rightarrow O_2^H + e$	$1.13\times10^{-15}\times\exp(-3.94/T_e)$	[9]
74	$e + O_2^*(b) \rightarrow O_2^H + e$	$1.13\times10^{-15}\times\exp(-2.31/T_e)$	[9]
75	$e + O_2^*(a) \rightarrow O_2^H + e$	$1.13\times10^{-15}\times\exp(-2.96/T_e)$	[9]
76	$O + O_2^H \rightarrow + O_2$	4.95×10^{-18}	[9]
77	$O + O_2^H \rightarrow O^* + O_2^*(b)$	1.35×10^{-18}	[9]
78	$O + O_2^H \rightarrow O^* + O_2^*(a)$	2.7×10^{-18}	[9]
79	$O_2 + O_2^H \rightarrow 2O_2^*(b)$	2.9×10^{-19}	[9]
80	$e + O_2^H \rightarrow + O^-$	$7.32\times10^{-16}\times T_e^{-1.072}\times\exp(-0.468/T_e)$	[9]
81	$e + O_2^H \rightarrow 2O + e$	$6.86\times10^{-15}\times\exp(-1.79/T_e)$	[9]

Table 3. The reaction set for oxygen reactions involving O_2^-.

	Reactions	Rate coefficients ($m^3 \cdot s^{-1}$)	References
82	$O_2^- + O_2^*(a) \rightarrow + O_2 + O_2$	2×10^{-16}	[9]
83	$O_2^- + O_2^*(b) \rightarrow + O_2 + O_2$	3.6×10^{-16}	[9]
84	$O_2^- + O \rightarrow O_2 + O^-$	1.755×10^{-16}	[17]
85	$O_2^- + O \rightarrow O_3 + e$	2.145×10^{-16}	[9]
86	$O_2^- + O_2^+ \rightarrow O_2 + O_2$	$2\times10^{-14}\times(T_g/300)^{0.5}$	[9]
87	$O_2^- + O_2^+ \rightarrow 2O + O_2$	$2\times10^{-14}\times(T_g/300)^{0.5}$	[9]
88	$O_2^- + O^+ \rightarrow + O_2$	$2\times10^{-14}\times(T_g/300)^{0.5}$	[9]
89	$O^- + O_3 \rightarrow O_2 + O_2^-$	0.3×10^{-15}	[9]
90	$O^- + O_2^*(a) \rightarrow + O_2^-$	4.75×10^{-17}	[9]
91	$e + O_3 \rightarrow + O_2^-$	$9.76\times10^{-14}\times T_e^{-1.309}\times\exp(-1.007/T_e)$	[9]
92	$O^- + O_2 \rightarrow + O_2^-$	4.75×10^{-18}	[43]

Table 4. Surface reactions and wall quenching and wall recombination coefficients.

	Reactions	γ	References
93	$O_2^*(a) \rightarrow O_2$	0.007	[17]
94	$O_2^*(b) \rightarrow O_2$	0.1	[17]
95	$O_2^H \rightarrow O_2$	0.1	[17]
96	$O \rightarrow \frac{1}{2}O_2$	$0.1438\times\exp(2.5069/p)$	[17]
97	$O^* \rightarrow \frac{1}{2}O_2$	$0.1438\times\exp(2.5069/p)$	[17]
98	$O^* \rightarrow O$	0.1	[17]
99	$Ar^* \rightarrow Ar$	0.1	[9]
100	$Ar^+ \rightarrow Ar$	$u_{B,Ar^+}\frac{A_{eff}}{V}$	[9]
101	$O_2^+ \rightarrow O_2$	$u_{B,O_2^+}\frac{A_{eff}}{V}$	[9]
102	$O^+ \rightarrow O$	$u_{B,O^+}\frac{A_{eff}}{V}$	[9]

Note: p is the pressure in unit mTorr.

3. Results and discussion

The reactions included in this simulation are classified into two control groups to explore the role of the three particles and related reactions in the Ar/O_2 discharge. The particle species considered in each group are presented in Table 5. Compared with case 1, case 2 takes into account three more particles $O_2\left(b^1\Sigma_g^+\right)$, $O_2\left(A^3\Sigma_u^+, A^3\Delta_u, c^1\Sigma_u^-\right)O_2^-$, and the corresponding reactions R_{57}–R_{92}, R_{94}–R_{95}.

In this work, one electrode is grounded, the other is driven by a single frequency source

$$V(t) = V_0\cos(\omega t), \tag{13}$$

where t is the time, $V_0 = 150$ V indicates the voltage amplitude, $\omega = 13.56$ MHz is the frequency. The electrode diameter is fixed at 15 cm, while the gap separation is 4.5 cm and the gas admixture is $Ar/O_2 = 50/50$.

Abundant active particles generated in Ar/O_2 plasma, including electrons, various ions, and neutral species, play significant roles in the plasma treatment process. Therefore, a detailed analysis will be conducted regarding the variations in charged particles and neutral species involved in this study for different pressures and collision reaction sets. As seen from Fig. 2, for different reaction sets, the electron temperature decreases as the pressure increases from 20 mTorr to 100 mTorr. The electron temperature calculated in case 2, which has a relatively comprehensive collision reaction set, shows little difference compared to the results calculated in case 1 at different pressures.

Table 5. Species included in two control groups in capacitively coupled Ar/O_2 mixed gas discharges.

Group number	Contained species
Case1	$Ar, Ar^*, Ar^+, O_2, O_2^*, O_3, O_2(a^1\Delta_g), O, O^*, O_2^+, O^+, O^-, e.$
Case2	$Ar, Ar^*, Ar^+, O_2, O_2^*, O_3, O_2(a^1\Delta_g), O, O^*, O_2^+, O^+, O^-, e, O_2, (b^1\Sigma_g^+), O_2(A^3\Sigma_u^+, A^3\Delta_u, c^1\Sigma_u^-), O_2^-$

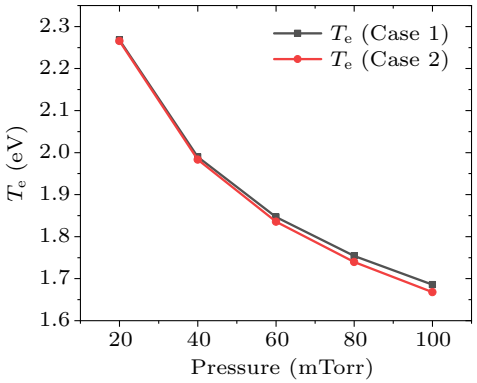


Fig. 2. Electron temperature as a function of the pressure for the two cases. Discharge condition: Ar/O_2 = 50/50 mixed gases with an electrode gap of 4.5 cm, sustained by 13.56 MHz with 150-V voltage amplitude.

Figure 3 shows the electron density and O^- density as a function of the pressure for different reaction sets. From Fig. 3, compared with case 1, the electron density and O^- density decrease a lot when $O_2(b^1\Sigma_g^+)$, $O_2(A^3\Sigma_u^+, A^3\Delta_u, c^1\Sigma_u^-)$, and O_2^- are included in the new reaction set. Moreover, the difference between the two cases become significant as the pressure increases. For example, a 18% reduction in electron density and a 43% reduction in O^- density can be found at 100 mTorr, respectively. With the increasing pressure, the electron density decreases first, and then reaches a minimum value at 40 mTorr. As the pressure increases further, the electron density starts to increase. This trend is consistent in both case 1 and case 2. However, the evolution of O^- density differs slightly in these two cases. In case 1, as the pressure increases, the O^- density increases first and then decreases. Similarly, the O^- density peaks at 40 mTorr. In contrast, O^- density decreases continuously with the increasing pressure in the case of new reaction set.

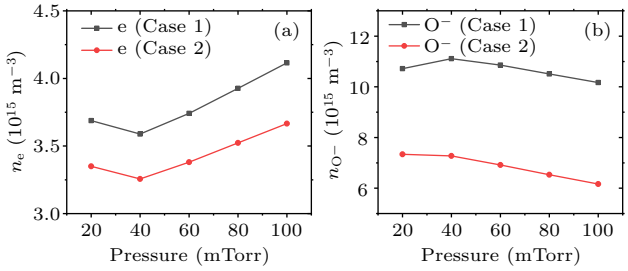


Fig. 3. Mean electron density (a) and O^- density (b) as a function of the pressure for the two cases. Discharge condition: Ar/O_2 = 50/50 mixed gases with an electrode gap of 4.5 cm, sustained by 13.56 MHz with 150-V voltage amplitude.

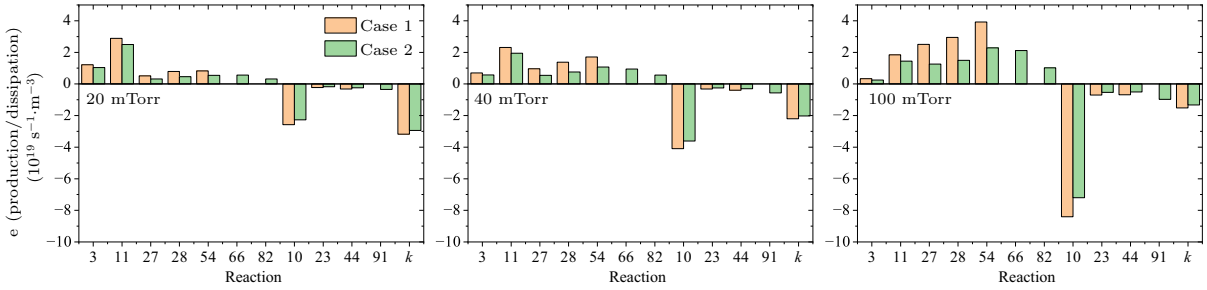


Fig. 4. Reaction rates for the generation and loss of electrons in the two cases for different pressures, k is the electron loss rate to the wall. Discharge condition: Ar/O_2 = 50/50 mixed gases with an electrode gap of 4.5 cm, sustained by 13.56 MHz with 150-V voltage amplitude. Note: The values of the horizontal coordinates correspond to those labeled in the reaction list.

A further investigation of variations of the electron and O^- densities is carried out by examining the changes of the reaction rates for the two cases, as shown in Figs. 4 and 5, in which, reactions that contribute less than 5% to the electron and O^- generation or loss are neglected. The positive terms mean the electron and O^- generation sources listed above the horizontal axis, while the loss terms are listed underneath the axis. According to the principle of electroneutrality, the electron loss rate to the wall is numerically equal to the sum of the wall losses of each positive ion. That is, it is the sum of the loss rates of reactions R_{100}, R_{101}, and R_{102}. As shown in Fig. 4, the relevant reaction rates are reduced when $O_2(b^1\Sigma_g^+)$, $O_2(A^3\Sigma_u^+, A^3\Delta_u, c^1\Sigma_u^-)$, and O_2^- are included. Particularly, the decrease in the generation rates is more pronounced. This reduction is primarily attributed to the newly added reaction R_{66}, which decreases the density of O^-, thereby weakens the rate of electron generation reactions (R_{27}, R_{28}, R_{54}). This mechanism results in a consistently lower electron density in case 2 than that in case 1.

Besides, the main reaction for the electron generation at low pressure is electron impact ionization of background gases Ar and O_2. Among them, reaction R_{11} contributes about 50% to electron generation at 20 mTorr. Furthermore, as the pressure increases, the electron impact ionization reaction rates

(R_3, R_{11}) slightly decrease at 40 mTorr, and meanwhile, the associative detachment reaction rate of O^- by $O_2\left(a^1\Delta_g\right)$ and O (R_{27}, R_{28}) as well as the detachment reaction rates (R_{54}, R_{66}, R_{82}) increase significantly. And at this pressure, the electron density reaches a minimum value. Moreover, the associative detachment reaction and detachment reaction become the most important reactions for the electron generation at 100 mTorr in both case 1 and case 2. For instance, the contribution of the detachment reaction (R_{54}, R_{66}, R_{82}) to the electron generation in case 2 is around 56%. In Liu[39]'s ICP investigation, it was believed that the electron impact ionization is the most important reaction for the electron generation with a fixed O_2 ratio of 20% and an applied power of 300 W, which is significantly different from our results. This is mainly because the electron temperature is higher in inductively coupled plasma discharges (ICPs) under the above discharge condition, which would enhance the electron impact ionization. The main reaction for electron loss is the dissociative attachment by O_2 (R_{10}). As the pressure increases to 100 mTorr, the reaction rate of R_{10} increases significantly. Meanwhile, there is an increase in the rate of the reactions (associative detachment reaction and detachment reaction) associated with the generation. This is probably why the electron density starts to increase as the pressure increases from 40 mTorr.

Figure 5 presents the reaction rates for the generation and loss of O^- in the two cases for different pressures. Compared with case 1, the rates of relevant reactions are all reduced when $O_2\left(b^1\Sigma_g^+\right)$, $O_2\left(A^3\Sigma_u^+, A^3\Delta_u, c^1\Sigma_u^-\right)$, and O_2^- are involved, as seen in Fig. 5. In terms of the O^- generation term, the addition of the R_{84} reaction plays a minor role. However, the addition of loss terms (R_{66}, R_{90}, R_{92}) play a vital role, causing the O^- density of case 2 consistently smaller than that in case 1. Gudmundsson[8] also found that the electron detachment from negative ion O^- by $O_2\left(b^1\Sigma_g^+\right)$ (R_{66}) significantly reduces the O^- density, which is consistent with our results.

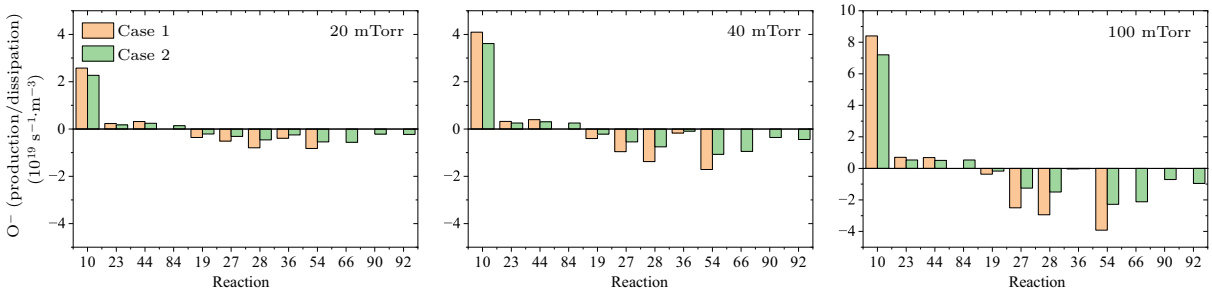


Fig. 5. Reaction rates for the generation and loss of O^- in the two cases for different pressures. Discharge condition: $Ar/O_2 = 50/50$ mixed gases with an electrode gap of 4.5 cm, sustained by 13.56 MHz with 150-V voltage amplitude. Note: The values of the horizontal coordinates correspond to those labeled in the reaction list.

The two groups of O^-densities show different trends under low pressure because O^- generation and loss reactions compete with each other. The main O^- generation reaction rate (R_{10}) increases as the pressure increases, which leads to an increase in O^- density at lower pressure (< 40 mTorr) for case 1. However, due to the added O^- loss reactions, O^- density decreases as the pressure increases at lower (< 40 mTorr) pressure in case 2. The change of the O^- density is dominated by an increase in the O^-loss reaction rate when the pressure increases from 40 mTorr to 100 mTorr. Besides, in both case 1 and case 2, dissociative attachment of the oxygen molecule (R_{10}) is almost the source of O^-, which contributes about 80% to O^- generation. The main loss reaction of O^- is the associative detachment of O^- by $O_2\left(a^1\Delta_g\right)$ and O (R_{27}, R_{28}) as well as detachment of O^- by $O_2\left(b^1\Sigma_g^+\right)$ and O_2 (R_{54}, R_{66}). Moreover, it can be found that the charge-exchange reaction (R_{90}, R_{92}) contributes about 19% to O^- loss at 100 mTorr in case 2.

Our findings contradict the claims made by the authors in Ref. [9] that the detachment reaction of O^- is not significant and R_{54} can be neglected in ICP operated Ar/O_2 discharges. Obviously, detachment of O^- by $O_2\left(b^1\Sigma_g^+\right)$ and O_2 plays a significant role in O^- loss and electron generation in Ar/O_2 CCP plasma. This also illustrates that the collision reaction path can be seriously modulated due to different heating mechanisms. Therefore, it is essential to evaluate the reaction sets for discharge sources.

Figure 6 shows the mean O_2^+ and Ar^+ densities as a function of the pressure for the two cases. Compared with case 1, the mean O_2^+ and Ar^+ densities are lower, when $O_2\left(b^1\Sigma_g^+\right)$, $O_2\left(A^3\Sigma_u^+, A^3\Delta_u, c^1\Sigma_u^-\right)$, and O_2^- are included. For example, the O_2^+ and Ar^+ densities drop by about 20% at 100 mTorr. Besides, as the pressure increases, Ar^+ density decreases, and O_2^+ density increases to a maximum value at 40 mTorr and then decreases.

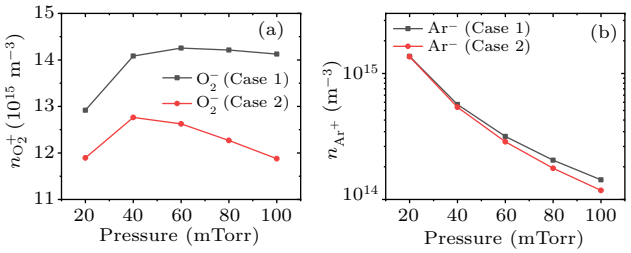


Fig. 6. Mean O_2^+ density (a) and Ar^+ (b) density as a function of the pressure for the two cases. Discharge condition: $Ar/O_2 = 50/50$ mixed gases with an electrode gap of 4.5 cm, sustained by 13.56 MHz with 150-V voltage amplitude.

In order to explain the variations of O_2^+, figure 7 presents

the reaction rates for the generation and loss of O_2^+ in the two cases for different pressures. Compared with case 1, all the reaction rates are reduced in case 2, particularly the electron impact ionization of O_2 (R_{11}). Obviously, the electron impact ionization of O_2 (R_{11}) is the most significant process for creating O_2^+, which contributes about 80% to O_2^+ generation in case 1 and case 2. This may be the main reason why the O_2^+ density in case 2 is lower than that in case 1. Moreover, the total O_2^+ generation rate decreases as the pressure increases. O_2^+ flux to the wall is the main loss term for O_2^+. Due to the decrease of the loss of recombination at the walls, the O_2^+ density increases at lower pressure (< 40 mTorr). At higher pressures (> 40 mTorr), a decreased reaction rate for the O_2^+ generation (R_{11}) contributes to the reduction in O_2^+ density. Besides, the charge exchange with O_2 (R_{32}) contributes roughly 20% to O_2^+ generation in case 1 and case 2. It is also noted that the ion–ion recombination with O^- (R_{19}, R_{51}) contributes about only 15% to O^- loss in case 1.

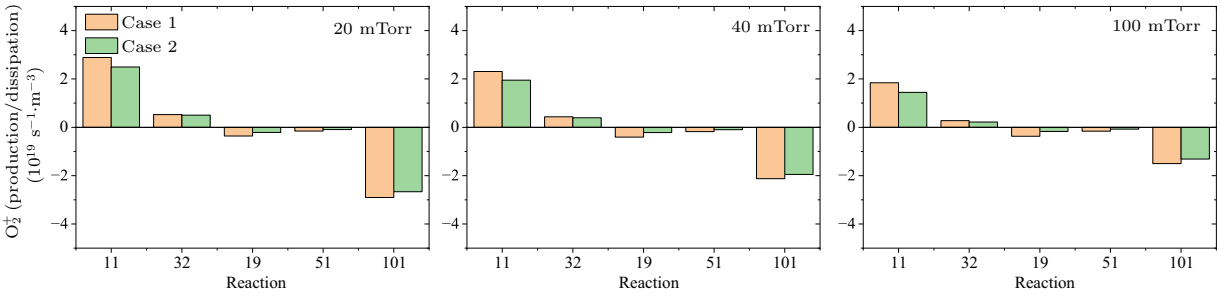


Fig. 7. Reaction rates for the generation and loss of O_2^+ in the two cases for different pressures. Discharge condition: $Ar/O_2 = 50/50$ mixed gases with an electrode gap of 4.5 cm, sustained by 13.56 MHz with 150-V voltage amplitude. Note: The values of the horizontal coordinates correspond to those labeled in the reaction list.

Figure 8 presents the reaction rates for the generation and loss of Ar^+ in the two cases for different pressures. It is seen from Fig. 8 that Ar^+ ions are mainly generated from the electron impact ionization of Ar (R_3). The main loss mechanism for Ar^+ is R_{32}, with roughly 38%–80% contribution for different pressures. However, at lower pressure (< 40 mTorr), R_{36} and the loss at the wall can not be neglected. Specifically, at 20 mTorr, R_{36} has about 30% contribution and the loss at the wall has roughly 25% contribution for the loss of Ar^+. The reduction in the electron temperature leads to a decreased reaction rate for R_3, consequently resulting in a lower in Ar^+ density in case 2 compared with case 1. Besides, as the pressure increases, the main generation reaction rate R_3 of Ar^+ decreases, which further leads to a decrease in Ar^+ density.

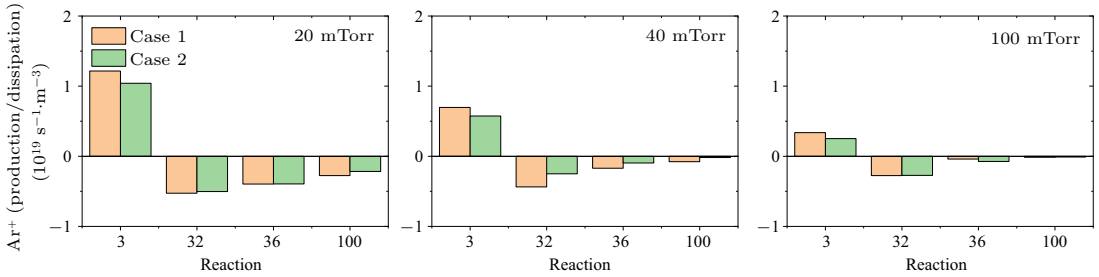


Fig. 8. Reaction rates for the generation and loss of Ar^+ in the two cases for different pressures. Discharge condition: $Ar/O_2 = 50/50$ mixed gases with an electrode gap of 4.5 cm, sustained by 13.56 MHz with 150-V voltage amplitude. Note: The values of the horizontal coordinates correspond to those labeled in the reaction list.

The O_2^- density and the corresponding reaction rates in case 2 for different pressures are shown in Fig. 9. O_2^- is a charged particle added in the new reaction set. The O_2^- density increases with the increasing pressure, and at 40 mTorr, it reaches a maximum value. When the pressure increases further, O_2^- density decreases. It can be also noted in Fig. 9(b) that, most of O_2^- originates from O^-, such as R_{90} and R_{92}, which contributes roughly 57% to the O_2^- generation. Meanwhile, the dissociative attachment by O_3 (R_{91}) contributes roughly 33% to O_2^- generation. The loss of O_2^- is mainly through detachment by $O_2\left(a^1\Delta_g\right)$ and $O_2\left(b^1\Sigma_g^+\right)$ (R_{82}, R_{83}). The charge exchange with O (R_{84}) and associative detachment by O (R_{85}) have roughly 15% and 25% contributions, respectively. At lower pressures (< 40 mTorr), the generation and loss rate of O_2^- are both increased, particularly the generation rate, which would cause the increase of O_2^- density at lower pressure (< 40 mTorr). As the pressure increases further the main loss reaction rate of O_2^- also increases significantly, leading to a decrease in O_2^- density at higher pressure (> 40 mTorr).

Figure 10 shows the mean densities of O, $O_2\left(a^1\Delta_g\right)$ and O^* as a function of the pressure for the two cases. Compared with case 1, the mean densities of O, $O_2\left(a^1\Delta_g\right)$ and O^* are lower in case 2. For example, the density of O^* in case 2 is about 45% lower. Besides, as the pressure increases, the mean densities of O and $O_2\left(a^1\Delta_g\right)$ increase, and meanwhile, the mean density of O^* decreases.

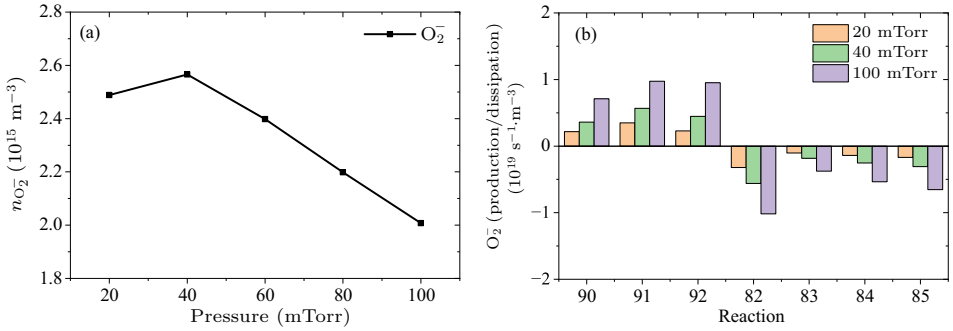


Fig. 9. Mean O_2^- density (a), reaction rates for the generation and loss of O_2^- (a) in case 2 for different pressures. Discharge condition: $Ar/O_2 = 50/50$ mixed gases with an electrode gap of 4.5 cm, sustained by 13.56 MHz with 150-V voltage amplitude. Note: The values of the horizontal coordinates correspond to those labeled in the reaction list.

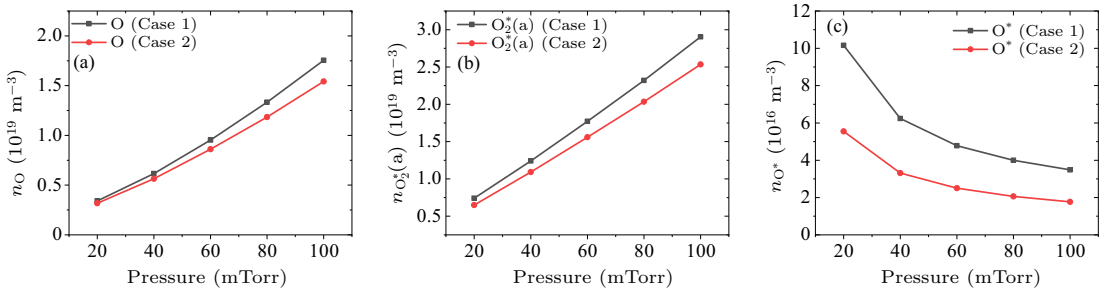


Fig. 10. Mean densities of O (a), O_2 ($a^1\Delta_g$) (b), and O^* (c) as a function of the pressure for the two cases. Discharge condition: $Ar/O_2 = 50/50$ mixed gases with an electrode gap of 4.5 cm, sustained by 13.56 MHz with 150-V voltage amplitude.

Figure 11 presents the reaction rates for the generation and loss of O in the two cases for different pressures. Obviously, the electron impact dissociation of O_2 (R_8, R_9) is the most significant process for the O generation, contributing about 60% to O generation in case 2. By contrast, the quenching of metastable atomic oxygen O^* by the O_2 molecule contributes roughly 21%, and the R_{59} contributes roughly 16% to O generation. Our conclusions regarding the main generation reactions of O differ significantly from those raised by Gudmundsson,[9] who considers the majority of ground state atomic oxygen O to be created by electron impact de-excitation of the metastable atom O^*. In this simulation, the loss at the wall is responsible for the most consumption, contributing more than 90% to O loss. Compared with case 1, despite the addition of R_{59} which can generate O, it was found that the rates of other O generation reactions in case 2 are reduced, which may be the main reason why O is lower in case 2 than that in case 1. Moreover, as the pressure increases, the O generation rates enhance. Therefore, this mechanism causes the increase of the mean O density.

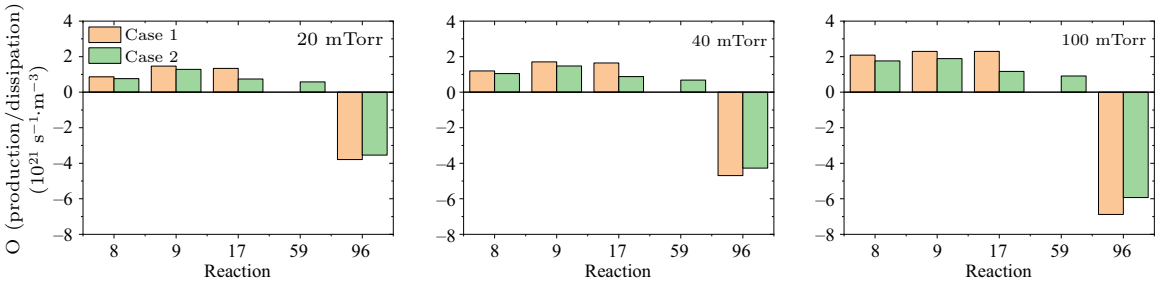


Fig. 11. Reaction rates for the generation and loss of O in the two cases for different pressures. Discharge condition: $Ar/O_2 = 50/50$ mixed gases with an electrode gap of 4.5 cm, sustained by 13.56 MHz with 150-V voltage amplitude. Note: The values of the horizontal coordinates correspond to those labeled in the reaction list.

Figure 12 presents the reaction rates for the generation and loss of $O_2\left(a^1\Delta_g\right)$ in the two cases for different pressures. From Fig. 12, the formation of $O_2\left(a^1\Delta_g\right)$ is dominated by the electron impact excitation (R_{22}). For the mechanism of loss, Toneli *et al.*[17] noted that the electron impact dissociation is the most important process in the loss of the metastable oxygen molecule $O_2\left(a^1\Delta_g\right)$ in the inductively coupled RF oxygen discharge. Nevertheless, in our results, wall quenching has important contributions for $O_2\left(a^1\Delta_g\right)$ loss, accounting for roughly 90% of the contribution. Compared with case 1, the main generation reaction rate R_{22} of $O_2\left(a^1\Delta_g\right)$ is lower, leading to a lower density of $O_2\left(a^1\Delta_g\right)$ in case 2. For example, there is a difference of about 13% in the $O_2\left(a^1\Delta_g\right)$ density at 100 mTorr, compared with case 1. The reaction rate R_{22} increases with the pressure, leading to an increase in $O_2\left(a^1\Delta_g\right)$ density.

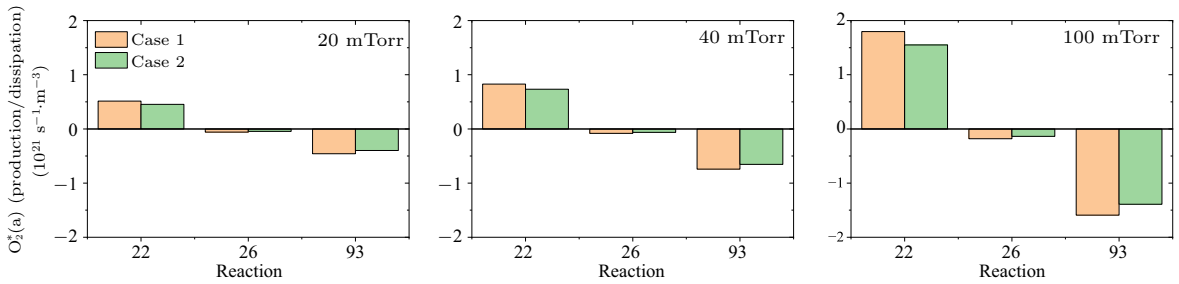


Fig. 12. Reaction rates for the generation and loss of O_2 ($a^1\Delta_g$) in the two cases for different pressures. Discharge condition: $Ar/O_2 = 50/50$ mixed gases with an electrode gap of 4.5 cm, sustained by 13.56 MHz with 150-V voltage amplitude. Note: The values of the horizontal coordinates correspond to those labeled in the reaction list.

Figure 13 presents the reaction rates for the generation and loss of O^* in the two cases for different pressures. From Fig. 13, the O^* generation only relates to the electron impact dissociation of O_2 (R_9). For the loss of O^*, it is mainly through quenching by the O_2 molecule. Moreover, R_{59} also contributes roughly 43% to O^* loss in case 2. Therefore, R_{59} cannot be neglected and need to be involved in the Ar/O_2 discharges. The O^* density is lower in case 2 than that in case 1. This reduction is primarily attributed to the newly added loss path R_{59}. Furthermore, as the pressure increases, the generation rate of R_9 enhances distinctly, which leads to an increase in O^* density.

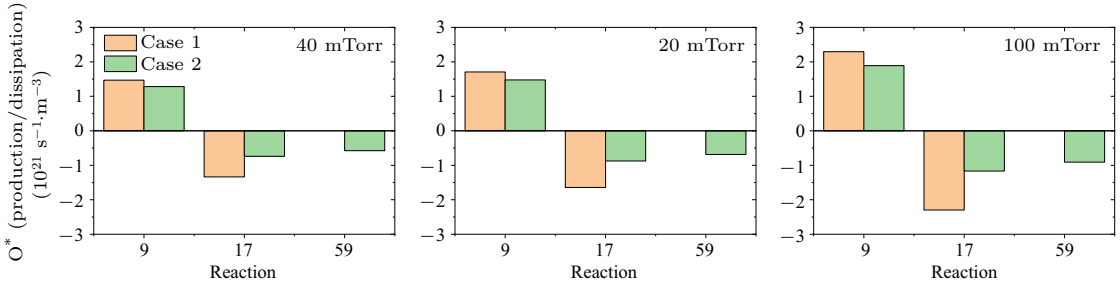


Fig. 13. Reaction rates for the generation and loss of O^* in the two cases for different pressures. Note: The values of the horizontal coordinates correspond to those labeled in the reaction list.

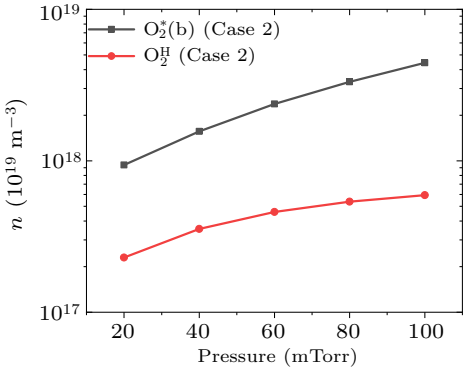


Fig. 14. Mean density of O_2 ($b^1\sigma_g^+$) (black solid line), O_2 ($A^3\Sigma_u^+$, $A^3\Delta_u$, $c^1\Sigma_u^-$) (red solid line) as a function of the pressure in case 2. Discharge condition: $Ar/O_2 = 50/50$ mixed gases with an electrode gap of 4.5 cm, sustained by 13.56 MHz with 150-V voltage amplitude.

Figure 14 shows the mean densities of $O_2\left(b^1\Sigma_g^+\right)$ and $O_2\left(A^3\Sigma_u^+, A^3\Delta_u, c^1\Sigma_u^-\right)$ as a function of the pressure in case 2. With the increasing pressure, the mean density of $O_2\left(b^1\Sigma_g^+\right)$ and $O_2\left(A^3\Sigma_u^+, A^3\Delta_u, c^1\Sigma_u^-\right)$ increase. Figure 15 presents the reaction rates for the generation and loss of $O_2\left(b^1\Sigma_g^+\right)$ and $O_2\left(A^3\Sigma_u^+, A^3\Delta_u, c^1\Sigma_u^-\right)$ as a function of the pressure. From Fig. 15, the most important reaction to the formation of the metastable oxygen molecule $O_2\left(b^1\Sigma_g^+\right)$ is R_{59}, which contributes about 76% at 20 mTorr. As the pressure increases, R_{58} and R_{79} become more important, for example, their contribution is about 24%, 25% at 100 mTorr, respectively. Wall quenching has an important contribution to $O_2\left(b^1\Sigma_g^+\right)$ loss, approximately 95%. The density of $O_2\left(b^1\Sigma_g^+\right)$ increases because the total generation rate increases with the increasing pressure. The generation of $O_2\left(A^3\Sigma_u^+, A^3\Delta_u, c^1\Sigma_u^-\right)$ is dominated by the electron impact excitation (R_{73}). It is important to note that the main $O_2\left(A^3\Sigma_u^+, A^3\Delta_u, c^1\Sigma_u^-\right)$ loss occurs from wall quenching at lower pressure. Nevertheless, the reaction rate of R_{79} and wall quenching contribute roughly 41% and 39% to the loss of $O_2\left(A^3\Sigma_u^+, A^3\Delta_u, c^1\Sigma_u^-\right)$ at 100 mTorr, respectively. The density of $O_2\left(A^3\Sigma_u^+, A^3\Delta_u, c^1\Sigma_u^-\right)$ increases because the generation rate R_{73} increases significantly as the pressure increases.

The average electronegativity as a function of the pressure for the two cases is seen in Fig. 16, which shows little difference at 20 mTorr. However, the averaged electronegativity is lower at higher pressure (> 40 mTorr) in case 2, and the difference between the two groups gradually increases as the pressure increases. The O^- density significantly decreases, especially at higher pressure, when $O_2\left(b^1\Sigma_g^+\right)$, $O_2\left(A^3\Sigma_u^+, A^3\Delta_u, c^1\Sigma_u^-\right)$, and O_2^- are included, resulting in a decrease in electronegativity compared with case 1. The average electronegativity increases to a peak value and then decreases as the pressure increases in case 1, showing a sig-

nificant difference from case 2, within the pressure range of 20 mTorr to 40 mTorr. At lower pressure, there is a slight decrease in electron density in both case 1 and case 2. In case 1, the O^- density increases at lower pressures, whereas, in case 2, the O^- density decreases. Although O_2^- shows an increasing trend within this pressure range, its density remains lower than that of O^-. Consequently, the primary contributors to the observed changes in electronegativity from 20 mTorr to 40 mTorr are electrons and O^-. And when the pressure increases further, the electron density increases and the negative ion (O^- and O_2^-) densities both decrease, which makes the electronegativity gradually decrease.

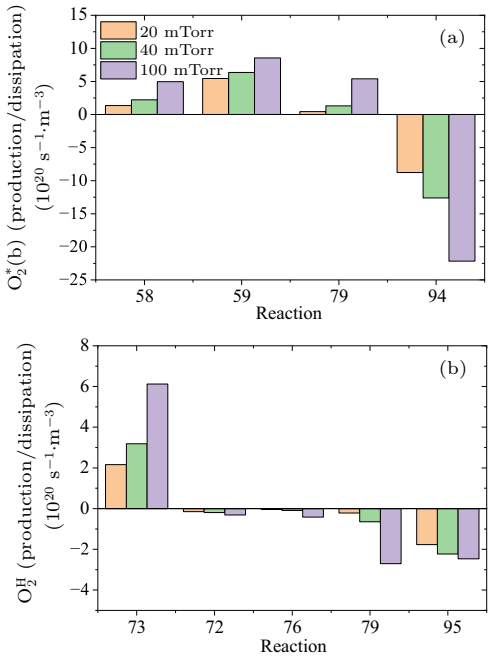


Fig. 15. Reaction rates for the generation and loss of O_2 ($b^1\Sigma_g^+$) (a), O_2 ($A^3\Sigma_u^+$, $A^3\Delta_u$, $c^1\Sigma_u^-$) (b) in case 2 for different pressures. Discharge condition: $Ar/O_2 = 50/50$ mixed gases with an electrode gap of 4.5 cm, sustained by 13.56 MHz with 150-V voltage amplitude. Note: The values of the horizontal coordinates correspond to those labeled in the reaction list.

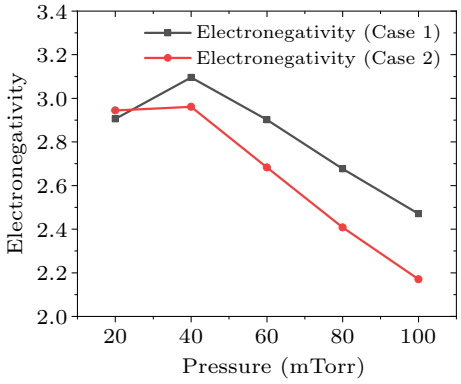


Fig. 16. The average electronegativity as a function of the pressure for the two cases. Discharge condition: $Ar/O_2 = 50/50$ mixed gases with an electrode gap of 4.5 cm, sustained by 13.56 MHz with 150-V voltage amplitude.

Figure 17 shows the time averaged voltage drop across the sheath and time-averaged charge within the sheath as a function of the pressure for the two cases. From Fig. 17, compared with case 1, the voltage drop across the sheath, which is significant for ion bombardment in surface processing, is enhanced in case 2. According to the formula $V_s = Q_s^2/2e\varepsilon_0 n_i^+ A^2$, charge Q_s within the sheath and the positive ion density n_i^+ determine the voltage drop across the sheath. Compared with case 1, the ion density and charge within the sheath are lower in case 2. Taking the result of 100 mTorr as an example, charge within the sheath Q_s is 8.447×10^{-8} C in case 1 and 7.804×10^{-8} C in case 2, respectively. This means the square of Q_s is decreased by 15% in case 2, compared with that in case 1. Besides, the total positive ion density is 1.428×10^{16} m^{-3} and 1.156×10^{16} m^{-3} respectively, showing a decrease of 19%. Therefore, the decrease in ion density leads to a higher sheath voltage drop in case 2 compared with the case 1. However, the square of Q_s and the ion density are decreased by 16% and 10%, respectively, as the pressure increases from 20 mTorr to 100 mTorr. This indicates that the reduction of charge within the sheath due to the increasing pressure is more pronounced, leading to a further decrease in the sheath voltage drop.

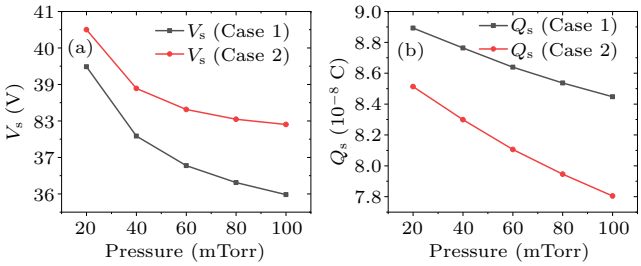


Fig. 17. Time-averaged voltage drop across the sheath V_s (a), time-averaged charge within the sheath Q_s (b) as a function of the pressure for the two cases.

The resistance of the plasma bulk region is an important physical quantity that characterizes the electrical conductivity of the plasma, and the change of the resistance directly determines the energy dissipation in the plasma, thus affecting the overall discharge efficiency. Figure 18 shows the inductance, the resistance of the plasma bulk, and the effective collision frequency ν_{eff} as a function of the pressure, in which the inductance and resistance are both enhanced in case 2 than those in case 1. As we know, a reduction in the electron density, as shown in Fig. 3(a), would lead to an increase in the inductance and resistance of the plasma bulk when $O_2\left(b^1\Sigma_g^+\right)$, $O_2\left(A^3\Sigma_u^+, A^3\Delta_u, c^1\Sigma_u^-\right)$, and O_2^- are included. As the pressure increases, the inductance of the plasma bulk increases first and then decreases. Besides, the effective collision frequency increases, which leads to an increase in resistance, as the pressure increases.

Based on the heating mechanism, the total absorbed power in plasma P_{abs} can be categorized into three parts, which are the Ohmic heating, stochastic heating, and sheath dissipation. Figure 19 shows the Ohmic heating P_{ohm}, stochastic heating P_{stoch}, sheath dissipation P_{sheath}, and total absorbed power in plasma in the two cases for different pressures. Compared

with case 1, $P_{\rm abs}$ and $P_{\rm sheath}$ decrease slightly, while $P_{\rm ohm}$ and $P_{\rm stoch}$ keep almost unchanged in case 2. As we know, $P_{\rm sheath}$ is mainly the energy gained by positive ions as they are accelerated by the voltage drop across the sheath. In case 2, the voltage drop across the sheath is higher than that in case 1, especially at higher pressures. But, $P_{\rm sheath}$ is also related to the radio frequency current $I_{\rm rf}(t)$ and the phase difference between $V_{\rm s}(t)$ and $I_{\rm rf}(t)$. $I_{\rm rf}(t)$ in case 2 is decreased compared to that in case 1. For example, The maximum value of current $I_{\rm rf}(t)$ is 3.594 A for case 1 and 3.389 A for case 2 at 100 mTorr. Besides, there is also a slight change in the phase difference between $V_{\rm s}(t)$ and $I_{\rm rf}(t)$ when comparing the two cases. Moreover, the $P_{\rm ohm}$ and $P_{\rm stoch}$ do not differ much from case 1 to case 2 at the same pressure. Therefore, the decrease of $P_{\rm abs}$ in case 2 is due to $P_{\rm sheath}$.

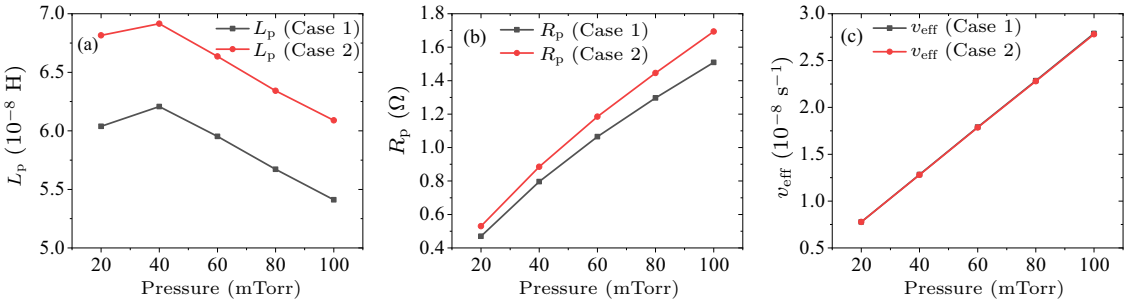


Fig. 18. The inductance (a) and the resistance (b) of the plasma bulk and the effective collision frequency (c) as a function of the pressure for the two cases.

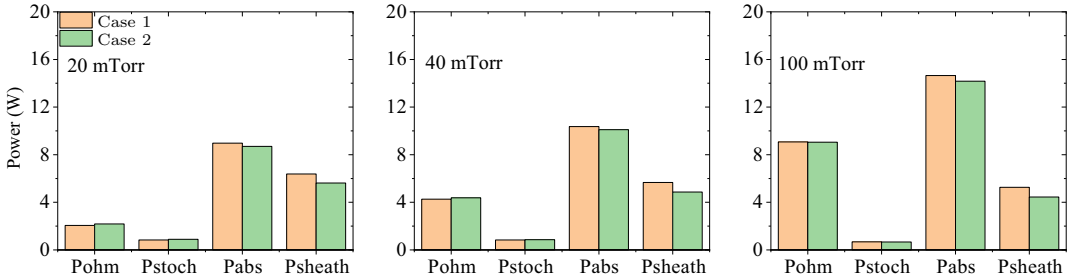


Fig. 19. Ohmic heating $P_{\rm ohm}$, stochastic heating $P_{\rm stoch}$, sheath dissipation $P_{\rm sheath}$, and total absorbed power in plasma $P_{\rm abs}$ in the two cases for different pressures.

Moreover, as the pressure increases, collisions between electrons and background neutral particles become more intense, resulting in a noticeable increase in $P_{\rm ohm}$. Meanwhile, from Fig. 17(a), the voltage drop across the sheath declines as the pressure increases, which might lead to a decrease in $P_{\rm sheath}$. Additionally, due to the significant enhancement in $P_{\rm ohm}$, the total absorbed power in plasma $P_{\rm abs}$ increases with the increasing pressure.

4. Conclusions

We have developed a plasma-equivalent circuit model coupled with a global model of the Ar/O_2 discharge, which allows us to determine the influence of newly added particles and reactions on the discharge properties in the pressure range from 20 mTorr to 100 mTorr. In this work, three particles $O_2\left(b^1\Sigma_g^+\right)$, $O_2\left(A^3\Sigma_u^+, A^3\Delta_u, c^1\Sigma_u^-\right)$, O_2^- and their corresponding reactions are added in the new reaction set. Compared to the previous reaction set, the RF period averaged electronegativity and electron temperature decrease. In addition, it is also shown that the sheath voltage drop, the inductance and resistance in the bulk are enhanced, and the total absorbed power in plasma $P_{\rm abs}$ and sheath dissipation $P_{\rm sheath}$ decrease slightly based on the new reaction set. Moreover, the difference between the two control groups becomes significant as the pressure increases.

In the new reaction set, the loss and generation channels of individual particles can be changed accordingly. The electron density and O^- density based on the new reaction set drop by about 18% and 43% at 100 mTorr, since the newly added detachment and charge-exchange reactions (R_{66} $O^- + O_2\left(b^1\Sigma_g^+\right) \rightarrow O_2 + O + e$, R_{90} $O^- + O_2\left(a^1\Delta_g\right) \rightarrow O + O_2^-$, R_{92} $O^- + O_2 \rightarrow O + O_2^-$) would cause the reduction of the density of O^-, and weaken the rates of electron generation reactions. Besides, it can be found that the detachment reactions become the most important reaction for the electron generation and O^- loss, especially at higher pressures (>40 mTorr). Reaction $O^* + O_2 \rightarrow O + O_2\left(b^1\Sigma_g^+\right)$ is crucial for both the generation of O and O^* losses, particularly at higher pressures, which contributes roughly 43% to O^* loss. And, due to the decreases in O^* density, the reaction rate $O_2 + O^* \rightarrow O_2 + O$ decreases, which causes the mean O density decrease. Thus, $O_2\left(b^1\Sigma_g^+\right)$ has a direct influence on the generation of electron and O, as well as the losses of O^- and O^*. The study also ex-

plores the generation and loss of O_2^- and $O_2\left(b^1\Sigma_g^+\right)$. Through the charge-exchange reactions, O_2^- can be generated, which also has a certain effect on O^- loss. Besides, the charge exchange with O_2 and $O_2\left(a^1\Delta_g\right)$ contributes roughly 57% to O_2^- generation. Meanwhile, dissociative attachment by O_2 contributes roughly 33% to O_2^- generation. The loss of O_2^- is mainly through detachment by $O_2\left(a^1\Delta_g\right)$ and $O_2\left(b^1\Sigma_g^+\right)$. The most important contribution to the formation of $O_2\left(b^1\Sigma_g^+\right)$ is energy transfer reaction R_{59} $(O^* + O_2 \rightarrow +O_2(b^1\Sigma_g^+))$, which has a 76% contribution at 20 mTorr. However, as the pressure increases, $R_{58}(e + O_2 \rightarrow O_2\left(b^1\Sigma_g^+\right) + e)$ and R_{79} $(O_2 + O_2\left(A^3\Sigma_u^+, A^3\Delta_u, c^1\Sigma_u^-\right) \rightarrow 2O_2\left(b^1\Sigma_g^+\right))$ become significant. Wall quenching has an important contribution for $O_2\left(b^1\Sigma_g^+\right)$ loss, which has roughly 95% contribution.

Additionally, from the simulation results in this work, it is necessary to evaluate the reactions in the specific simulations rather than applying the reactions from different discharge sources. Finally, it is expected that the results in this work can provide references for future simulations.

Acknowledgement

Project supported by the National Natural Science Foundation of China (Grant Nos. 12020101005, 12475202, 12347131, and 12405289).

References

[1] Qu C, Sakiyama Y, Agarwal P and Kushner M J 2021 *J. Vac. Sci. Technol. A* **39** 052403
[2] Nagamine M, Itoh H, Satake H and Toriumi A 1998 *International Electron Devices Meeting* pp. 593–596
[3] Fang G Y, Xu L N, Cao Y Q, Wang L G, Wu D and Li A D 2015 *Chem. Commun.* **51** 1341
[4] Kitajima T, Nakano T and Makabe T 2008 *J. Vac. Sci. Technol. A* **26** 1308
[5] Gudmundsson J T and Lieberman M A 2015 *Plasma Sources Sci. Technol.* **24** 035016
[6] Gibson A R and Gans T 2017 *Plasma Sources Sci. Technol.* **26** 115007
[7] Hannesdottir H and Gudmundsson J T 2016 *Plasma Sources Sci. Technol.* **25** 055002
[8] Gudmundsson J T and Snorrason D I 2017 *J. Appl. Phys.* **122** 193302
[9] Gudmundsson J T and Thorsteinsson E G 2007 *Plasma Sources Sci. Technol.* **16** 399
[10] Lichtenberg A J, Vahedi V, Lieberman M A and Rognlien T 1994 *J. Appl. Phys.* **75** 2339
[11] Chung T H 1999 *J. Korean Phys. Soc.* **34** 24
[12] Gudmundsson J T 2004 *J. Phys. D: Appl. Phys.* **37** 2073
[13] O'Brien Jr R J and Myers G H 1970 *J. Chem. Phys.* **53** 3832
[14] Burrow P D 1973 *J. Chem. Phys.* **59** 4922
[15] Proto A and Gudmundsson J T 2018 *Plasma Sources Sci. Technol.* **27** 074002
[16] Thorsteinsson E G and Gudmundsson J T 2010 *Plasma Sources Sci. Technol.* **19** 055008
[17] Toneli D A, Pessoa R S, Roberto M and Gudmundsson J T 2015 *J. Phys. D: Appl. Phys.* **48** 325202
[18] Derzsi A, Vass M, Masheyeva R, Horvath B, Donko Z and Hartmann P 2024 *Plasma Sources Sci. Technol.* **33** 025005
[19] Lim N, Efremov A and Kwon K H 2021 *Plasma Chem. Plasma Process.* **41** 1671
[20] Park G and Lee H J 2020 *IEEE International Conference on Plasma Science (ICOPS)*, p. 589
[21] Lee M Y, Jung J, Kim T W, Kim K H, Kwon D C and Chung C W 2020 *Phys. Plasmas* **27** 115002
[22] Nikolić M, Sepulveda I, Gonzalez C, Khogeer N and Fernandez-Monteith M 2021 *J. Phys. D: Appl. Phys.* **54** 275203
[23] Krüger F, Lee H, Nam S K and Kushner M J 2021 *Plasma Sources Sci. Technol.* **30** 085002
[24] Liu J, Zhang Q Z, Liu Y X, Gao F and Wang Y N 2013 *J. Phys. D: Appl. Phys.* **46** 235202
[25] Wang L, Wen D Q, Zhang Q Z, Song Y H, Zhang Y R and Wang Y N 2019 *Plasma Sources Sci. Technol.* **28** 055007
[26] Derzsi A, Bruneau B, Gibson A R, Johnson E, O'Connell D, Gans T, Booth J P and Donkó Z 2017 *Plasma Sources Sci. Technol.* **26** 034002
[27] Gao Z Y, Dong W, Tian C B, Jiang X Z, Dai Z L and Song Y H 2024 *Chin. Phys. B* **33** 095203
[28] Wang L, Wen D Q, Tian C B, Song Y H and Wang Y N 2021 *Acta Phys. Sin.* **70** 095214 (in Chinese)
[29] Lieberman M A and Lichtenberg A J 2005 *Principles of Plasma Discharges and Materials Processing*, 2nd edn. (New York: Wiley-Interscience) pp. 1–750
[30] Bora B, Bhuyan H, Favre M, Wyndham E, Chuaqui H and Kakati M 2011 *Phys. Plasmas* **18** 103509
[31] Schmidt F, Mussenbrock T, Trieschmann J 2018 *Plasma Sources Sci. Technol.* **27** 105017
[32] Bora B 2015 *Plasma Sources Sci. Technol.* **24** 054002
[33] Bora B and Soto L 2014 *Phys. Plasmas* **21** 083509
[34] Bai X, Xu H W, Tian C B, Dong W, Song Y H and Wang Y N 2023 *Chin. Phys. B* **32** 125203
[35] Mussenbrock T, Brinkmann R P, Lieberman M A, Lichtenberg A J and Kawamura E 2008 *Phys. Rev. Lett.* **101** 085004
[36] Bora B, Bhuyan H, Favre M, Wyndham E and Chuaqui H 2012 *Appl. Phys. Lett.* **100** 094103
[37] Donkó Z, Schulze J, Czarnetzki U and Luggenhölscher D 2009 *Appl. Phys. Lett.* **94** 131501
[38] Bora B, Bhuyan H, Favre M, Wyndham E and Wong C S 2013 *J. Appl. Phys.* **113** 153301
[39] Liu W, Wen D Q, Zhao S X, Gao F and Wang Y N 2015 *Plasma Sources Sci. Technol.* **24** 025035
[40] Thorsteinsson E G and Gudmundsson J T 2009 *Plasma Sources Sci. Technol.* **19** 015001
[41] Thorsteinsson E G and Gudmundsson J T 2010 *J. Phys. D: Appl. Phys.* **43** 115201
[42] Hsu C C, Nierode M A, Coburn J W and Graves D B 2006 *J. Phys. D: Appl. Phys.* **39** 3272
[43] Turner M M 2015 *Plasma Sources Sci. Technol.* **24** 035027